ORIGINAL RESEARCH

CrossMark

Ni and Ni_xCo_y Alloys Electrodeposited on Stainless Steel AISI 316L for Hydrogen Evolution Reaction

Melisa J. Gomez [1] · Esteban A. Franceschini [1] · Gabriela I. Lacconi [1]

Abstract

Ni_xCo_y electrocatalysts for hydrogen evolution reaction (HER) were synthesized by electrodeposition on AISI 316L stainless steel (denoted as SS316L), as a scalable and economical alternative to be used in alkaline electrolyzers. For this, a previous treatment of the SS316L surface was carried out in order to optimize the deposition of different catalytic films containing Ni and Ni_xCo_y with different compositions ($Ni_{89}Co_{11}$, $Ni_{69}Co_{31}$, and $Ni_{29}Co_{71}$). The properties of the catalysts were established by scanning electron microscopy (SEM), energy-dispersive X-ray spectroscopy (EDS), and X-ray diffraction (XRD), and the catalytic activity for HER was evaluated by potentiodynamic experiments in 1 M KOH solutions. An increase in the current density toward the hydrogen evolution reaction was found with these Ni_xCo_y electrodes. For the $Ni_{69}Co_{31}$ catalyst, current density values 112% higher than those recorded with deposited Ni from conventional Watts bath were obtained. The HER current shows a strong dependence on the content of Co on the alloy that is also evidenced in the electrochemical impedance experiments. The efficiency of electrocatalytic activity for HER was increased after an electrochemical aging treatment, indicating the presence of an activation process, for example with $Ni_{89}Co_{11}$ electrodes, where higher current density for HER was observed.

Keywords Hydrogen evolution reaction · Alkaline electrolysis · Electrodeposition · Nickel · Nickel cobalt

Introduction

Hydrogen has acquired relevance as energy vector in the last decades because it is one of the cleanest ways to store energy generated by different sources, including renewable ones [1–23], particularly in countries with large territorial extensions where energy distribution can be complicated and costly.

The production of hydrogen can be carried out via a wide diversity of methods, among which electrolysis is the one that provides the purest product [4, 5]. The conventional electrolyzer works in alkaline media with metallic electrodes, such as pure nickel plates normally used as catalyst for the hydrogen evolution reaction [6, 7].

It is well known that the electrodeposited metals and alloys have higher hardness than that obtained by conventional metallurgical processes [8, 9]. Although the electrodeposition technology by potential pulse application has been developed since some decades, the pulse electroplating process is a relatively novel methodology that allows obtaining different superficial textures on metals and alloys. In the traditional direct current (DC) electroplating, the metal ions are reduced in the cathode, generating a concentration gradient near the electrode/electrolyte interface, which causes the subsequent roughness of the surface.

AISI 316L stainless steel (denoted as SS316L) is one of the most commonly employed steels used in high corrosive environments, due to its inherent resistance properties attributed to the spontaneous formation of a thin, adherent, and self-healing passive film on the surface [10, 11]. For that reason, SS316L is widely used in chemical processing, biomaterial, petrochemical, and nuclear industries.

✉ Esteban A. Franceschini
estebanfranceschini@yahoo.com.ar

✉ Gabriela I. Lacconi
glacconi@fcq.unc.edu.ar

[1] INFIQC-CONICET, Dto. de Fisicoquímica, Facultad de Ciencias Químicas, Universidad Nacional de Córdoba, Ciudad Universitaria, 5000 Córdoba, Argentina

Moreover, the calculated production cost in Argentina indicates that a pure nickel electrode costs U$S 1324 per square meter, while the price of an electrodeposited nickel on SS316L electrodes is about U$S 489 (per m^2). This represents a savings of approximately 63% without risking the amount of production.

The typical electrodeposition baths used for nickel-based alloy plating are those with sulfate, sulfamate, Watts, and chloride-type baths [12]. In the case of Ni-Co electrodeposited alloys, it is common to find references dealing with anomalous composition [13–16]. Ni-Co alloys were found to have distinctive mechanical, thermophysical, and magnetic properties [8, 17]. Thus, Ni-Co alloys have a bright dark metal appearance, and compared with pure nickel, the deposit has higher hardness and better wear resistance, corrosion resistance, and chemical stability. In addition, Ni-Co electrodeposited alloys are also very suitable for the preparation of composite coatings [18], which transform these catalysts in excellent platforms to the development of advanced structured catalysts.

Kautek and coworkers [19] synthesized and characterized a variety of Ni-Co electrodeposits on steel using a 5-A-dm^2 current pulse. They observed that the choice of the counterion strongly influences the reaction mechanism, and as a consequence, the properties of the deposited alloy can be modified. Also, the cobalt content of the alloy is strongly dependent on the electrolyte system used. While sulfamate and Watts baths show ability for surface passivation, the chloride bath exhibits a lower passivation proneness, accompanied by pit formation on the surface.

Lupi et al. [20] synthesized Ni-Co alloys of various Co compositions ranging from 0 to 100% by electrodeposition on aluminum net supports. The alloys were examined by polarization measurements. The decomposition voltage and the hydrogen overpotential appear to be lower in the case of Co concentrations between 41 and 64 wt%, where the synergism among the catalytic properties of nickel (low hydrogen overpotential) and of cobalt (high hydrogen adsorption) is best achieved and which allows to obtain a larger value of the exchange current density. It is important to note that this article does not analyze the influence of the electroplating bath composition, so that, taking into account the work of Kautek and coworkers [19] where it explains the effect of the counterions in the bath on the surface properties of the coating formed, it makes impossible an analysis of the applicability of the catalysts synthesized by Lupi.

In this work, we proposed to replace most of the volume of the conventional nickel electrode by stainless steel AISI 316L which is a cheap and resistant material to be used in alkaline electrolyzers. In that way, a pretreatment for SS AISI 316L was developed and different nickel-based catalysts were synthesized by electrodeposition on the steel. Characterization of the structure and composition of the electrode, in addition to the analysis electrocatalytic response, was performed in order to obtain a high activity catalyst for HER, with low cost, diminishing the cost of the produced hydrogen production.

Experimental

Materials Used

Hydrochloric acid (Cicarelli, PA grade), potassium hydroxide (Anedra RA reagent), nitric acid (Cicarelli, PA grade), sulfuric acid (Cicarelli, PA grade), nickel sulfate (Anedra, PA grade), nickel chloride (Merck, PA grade), boric acid (Merck, PA grade), and ethanol (Cicarrelli) were used as received without further purification. All solutions were prepared with Milli-Q water and degassed using high purity N_2 (Indura S.A.). AISI 316L SS plates with dimensions of $20 \times 35 \times 2.5$ mm were used as the substrates. The stainless steel AISI 316L (denoted as SS316L) was covered with insulating tape so that a 4-cm^2 area remains uncovered. The composition of the SS316L was Cr 17%, Ni 12%, C 0.01%, Mn 2%, Si 0.75%, P 0.045%, S 0.03%, Mo 2.50%, and Fe% Bal.

Solution and Sample Preparation

The substrate surface was pretreated in order to prepare it for the electrodeposition process. First, the plates were polished with #600 sandpaper for 6 min, obtaining an average roughness of 0.09 ± 0.01 μm (determined by confocal microscopy as is explained below). Then, the samples were sonicated for 30 min in acetone and rinsed with ethanol and Milli-Q water. After that, immersion in 1.0 M KOH aqueous solution at 323 K (15 min) was performed for degreasing the steel, and then an anodic current pulse of 1 mA cm^{-2} for 15 min in 1.0 M nitric acid was applied to the electrode to oxidize any organic trace on the surface. Finally, successive immersions of the sample in 1.0 M KOH, 13.2 w/v % HCl, and 5 w/v % H_2SO_4 for 1 min each to deoxidize and activate the surface were carried out.

This preparation is crucial since if it is not carried out, the first electrodeposited layer of nickel is visibly thinner which indicates that it does not have a good adhesion to the steel. Especially the electrolytic cleaning step provides an oxide-free surface which ensures better adhesion of the metal and greater reproducibility of the electrodes obtained [21].

Three types of plating baths were prepared for the electrodeposition on the steel. The first bath promotes conditions on the surface for improving the metallic adherence and, as a consequence, increasing the stability of the subsequent electrodeposit. This adhesion layer was obtained using a 225 g/L $NiCl_2 \cdot 6H_2O$ solution acidified to pH 0.5 with HCl. The second bath, employed for the synthesis of Ni Watts catalytic layers, has the composition of the conventional Watts bath: 280 g/L $NiSO_4 \cdot 6H_2O$, 35 g/L $NiCl_2 \cdot 6H_2O$, and 45 g/L H_3BO_3 at pH = 3.5. The third one was used to synthesize the Ni_xCo_y catalysts, and it was prepared with 280 g/L $NiSO_4 \cdot 6H_2O$, 45 g/L H_3BO_3, and different quantities of $CoSO_4 \cdot 7H_2O$ to obtain baths with molar Ni/Co ratios of 85/15, 96.5/3.5, and

98.5/1.5 with pH of 1.5, 3, and 3.5, respectively. The pH values of the electrolytes were found to be strongly dependent on the Co concentration.

Nickel electrodeposition in every step was performed in a two-electrode cell with a nickel anode, by application of a − 0.05-A/cm² pulse at 55 °C, during 1800 s for the adherence layer and 2700 s for the catalytic layer. The total coating thickness is about 75 μm, which includes 30 μm from the adhesion layer and 45 μm of the catalytic layer.

Characterization

Scanning electron images were measured employing a Supra 40 (Zeiss Company) FESEM operating at 3–6 kV, equipped with EDX operating at 6–15 kV.

X-ray diffractograms were obtained using the Cu Kα radiation ($\lambda = 1.5406$ Å), with a PANalytical X'Pert PRO diffractometer (40 kV, 40 mA), for the θ–2θ Bragg–Brentano geometry. The 2θ range used was from 10° to 70°, with steps of 0.02° and a counting time of 1 s per step. The FULLPROF program [22] was employed to refine the crystal structure by the Rietveld method. The data refined were lattice parameters, peak shape, atomic positions, isotropic thermal parameters, and occupation factors.

Raman spectra of the electrodes surface were obtained using a Horiba Jobin-Yvon Raman microscope (LABRAM-HR), with a ×100 objective lens (NA = 0.9). The illuminated area was 1.0 μm² with a 488.0 nm laser (Ar laser) and spectral resolution of 1.5 cm⁻¹, and the power of radiation was 3.5 mW at the sample. The homogeneity of the catalysts was corroborated measuring in different zones of each sample.

Confocal microscopy images were obtained using an Olympus LEXT OLS4000 employing a 405 nm wavelength laser, magnifications of ×1070 and ×2132, with a pitch in the z-axis of 0.05 and 0.01 μm with areas for data collection of 258 and 130 μm², respectively.

The electrochemical experiments for the HER evaluation were carried out in a conventional three-electrode electrochemical cell. A large area platinum sheet was employed as counter electrode and a saturated calomel electrode (SCE) as reference electrode (0.243 V vs. RHE). The reference electrode was included into a capillary and kept at room temperature. The aqueous electrolyte was 1.0 M KOH solution. All the electrochemical studies were performed with an Autolab potentiostat/galvanostat model PGStat30 with FRA2 module. The uncompensated ohmic corresponding to the electrolyte resistance (∼ 50 Ω) was measured via high-frequency ac impedance in N₂-saturated 1 M KOH solutions, a value that was used to calculate the cell constant. The ohmic drop correction was automatically performed by Autolab software (Metrohm Autolab Nova 1.10). The electrolyte temperature was controlled by a Lauda Alpha RA 8 thermostat, at temperatures between 298 and 323 K.

Results and Discussion

Structural and Chemical Characterization

Nickel Adhesion Layer

The adhesion layer of nickel is obtained by a galvanostatic pulse (− 0.05 A/cm²) in a 225 g/L NiCl₂ solution, pH 0.5 at 55 °C during 1800 s.

The nickel adhesion layers were characterized by various microscopy techniques in order to analyze their structure. Confocal microscopy images (not shown) were taken in order to determine the surface uniformity (denoted as RMS of the adhesion layers).

RMS is defined as the square root of the mean of the squares of the ordinates of the effective profile in relation to the midline in a measurement module. This makes it very susceptible to the presence of inhomogeneities on the surface since, when they are squared, these point values substantially increase the RMS.

Values of RMS were around 0.42 μm in all experiments with very high reproducibility. In Fig. 1a, the SEM micrograph of the nickel adhesion layer shows a granular structure with a relatively high roughness which is according with the RMS calculated through the confocal microscopy measurements.

X-ray diffractograms of nickel adhesion layers exhibit the characteristic reflection peaks for crystalline nickel with a face-centered cubic (fcc) structure [23]. The 2θ values for the Ni (1 1 1) and (2 0 0) planes are 44.5° (FWHM = 0.255°) and 51.9° (FWHM = 0.128°), respectively, with a d-spacing distance of 2.03 Å for the plane (1 1 1) and 1.76 for the (2 0 0) plane. Furthermore, the (1 1 1)/(2 0 0) intensity ratio of the Ni XRD peaks is 1.31, showing a preferential (1 1 1) plane [23].

Nickel and Nickel/Cobalt Catalytic Layers

Confocal microscopy images were taken on all samples to determine the surface roughness. The obtained values of RMS are presented in Table 1.

Changes in RMS ranging from 0.40 to 0.25 μm can be observed depending on the sample. The $Ni_{89}Co_{11}$ and $Ni_{69}Co_{31}$ electrodes have lower RMS values, decreasing in the above order, values that are indicative of a major surface uniformity. Although the differences found are not negligible, they do not greatly affect the electrocatalytic activity, in fact, and as will be seen in the following sections, even the samples with lower RMS present higher current densities for hydrogen generation. This feature indicates that the changes in the RMS, although it is an approximated measure of the catalyst surface area, are not a determinant of its activity, being able to have a high activity in spite of the smaller RMS. It is important to clarify that the values of RMS found in the different samples of the same catalyst are reproducible.
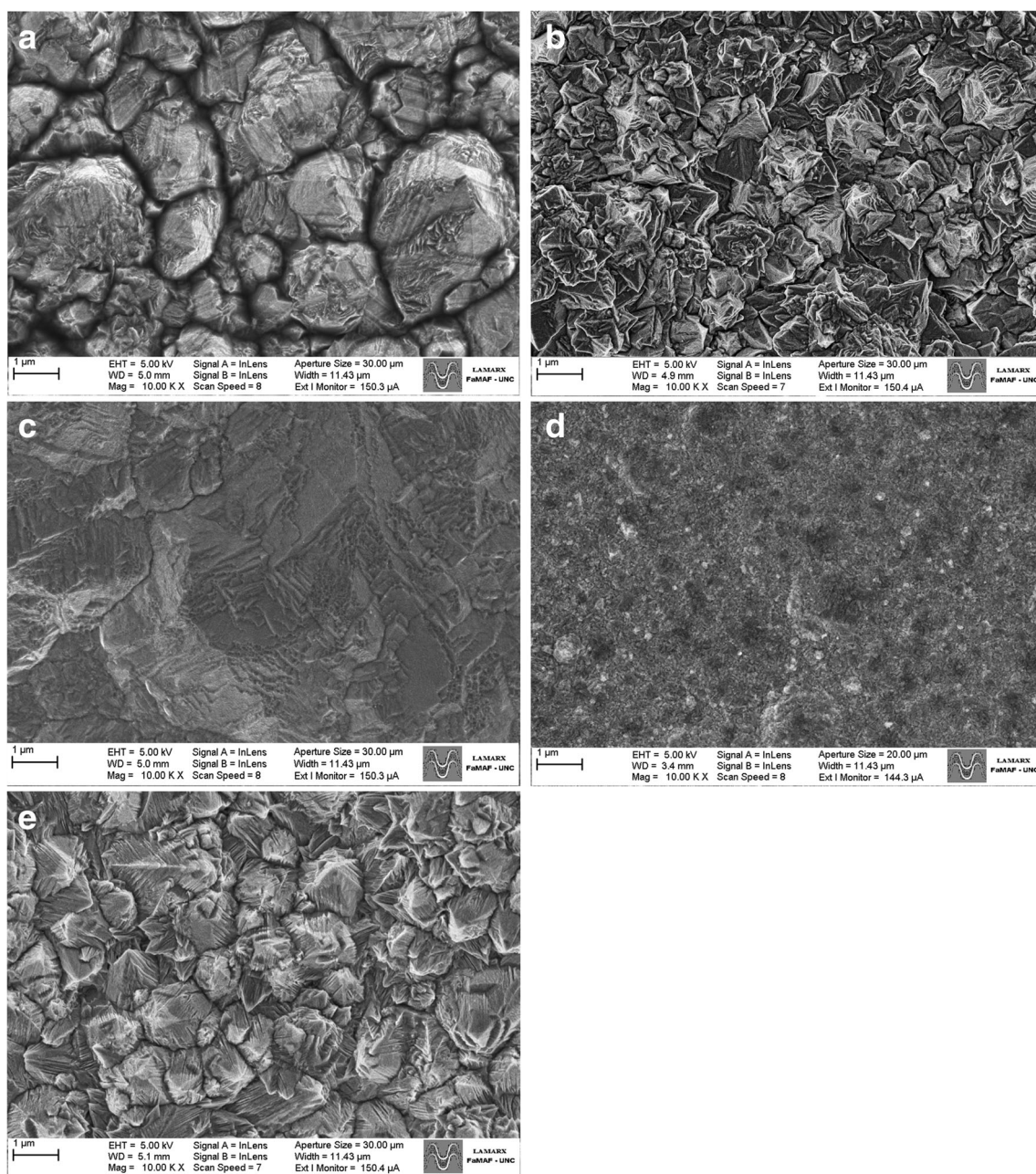
Fig. 1 SEM micrographs measured at 5 keV and a magnification of ×10,000 of **a** nickel adhesion layer, **b** Ni deposited from Watts bath, and Ni alloys deposited from Watts-modified bath: **c** $Ni_{89}Co_{11}$, **d** $Ni_{69}Co_{31}$, and **e** $Ni_{29}Co_{71}$

Figure 1b–e shows the SEM images of nickel Watts and Ni_xCo_y alloy electrodeposited catalysts. It can be seen that all the catalysts have a layered granular structure with grains of different sizes, depending on their chemical composition. On the other hand, the values of RMS correspond to the samples that present structures with smaller grains. The EDS spectra were measured on the Ni Watts and Ni_xCo_y samples in order to determine the composition of the catalysts, and its analysis is presented in Table 1. No significant deviations were found on different regions of the samples, and the measured Co contents were systematically higher than the nominal composition of the

precursor in the electrodeposition bath, even though cobalt presents a more negative reduction potential than nickel (− 0.27 and − 0.25 V, respectively) [20]. These results indicate that cobalt, being the less noble metal, is preferentially deposited, a feature that can produce an inhibition effect on the growth of crystalline nickel alloys [20]. Another possible explanation proposed by Bai et al. for this phenomenon is related to the formation of hydrogen during the electrolysis, as it enhances the formation of metal hydroxyl in the coating surface [24]. The tendency of OH^- ion inclusion in the metal coating is facilitated in chloride solutions, while it is lower in sulfate and sulfamate

Table 1 Composition (expressed as % mol) of the synthesized catalysts obtained by EDS, compared with the nominal composition of electrodeposition bath

Nominal % mol		EDS % mol		RMS (μm)
Ni	Co	Ni	Co	
100	0	100	0	0.43
98.5	1.5	89	11	0.32
96.5	3.5	69	31	0.24
85	15	29	71	0.41

solutions. On the other hand, Machado and coworkers suggest that in the case of Ni-Co alloy deposition, the ability for the adsorption of $Co(OH)^+$ species is higher than that of $Ni(OH)^+$ [13, 14]. Therefore, the Ni-Co alloy gets rich in Co resulting in an anomalous deposition.

Figure 2b shows the XRD patterns for Ni alloys with different contents of Co in comparison with the Ni Watts deposit pattern. Ni Watts deposits have a similar pattern to that of the adherence Ni layer (Fig. 2a) with the presence of typical

reflections of face-centered cubic nickel at 44.5° and 51.9° 2θ values for Ni (1 1 1) and (2 0 0) planes, respectively [23].

The values of 2θ for the Ni (1 1 1) and (2 0 0) planes for all the catalysts vary with the Co content and are presented in Table 2. The Ni_xCo_y alloy cell parameters and average crystal size were calculated using Scherrer's equation [25, 26]. Figure 2c, d shows magnifications of the characteristic zone for the normalized (1 1 1) and (2 0 0) plane peaks, respectively. It is clearly observed that the increase of Co content in the Co ratio of the alloy affects the peaks' positions by shifting them toward smaller angles, when the amount of Co in the alloy is increased. These results are associated with an increase of the d parameter, presented in Table 2. Particularly, the peak corresponding to the (1 1 1) plane in the $Ni_{29}Co_{71}$ catalyst is clearly formed by two peaks indicating a nonclearly defined structure confounded by the various crystals with different structures. This may be due to the high proportion of Co in the sample, causing the presence not only of the nickel peaks but also of the Co peaks [27, 28].

The Raman spectra of the freshly synthesized catalysts are presented in Fig. 3. There are no significant differences
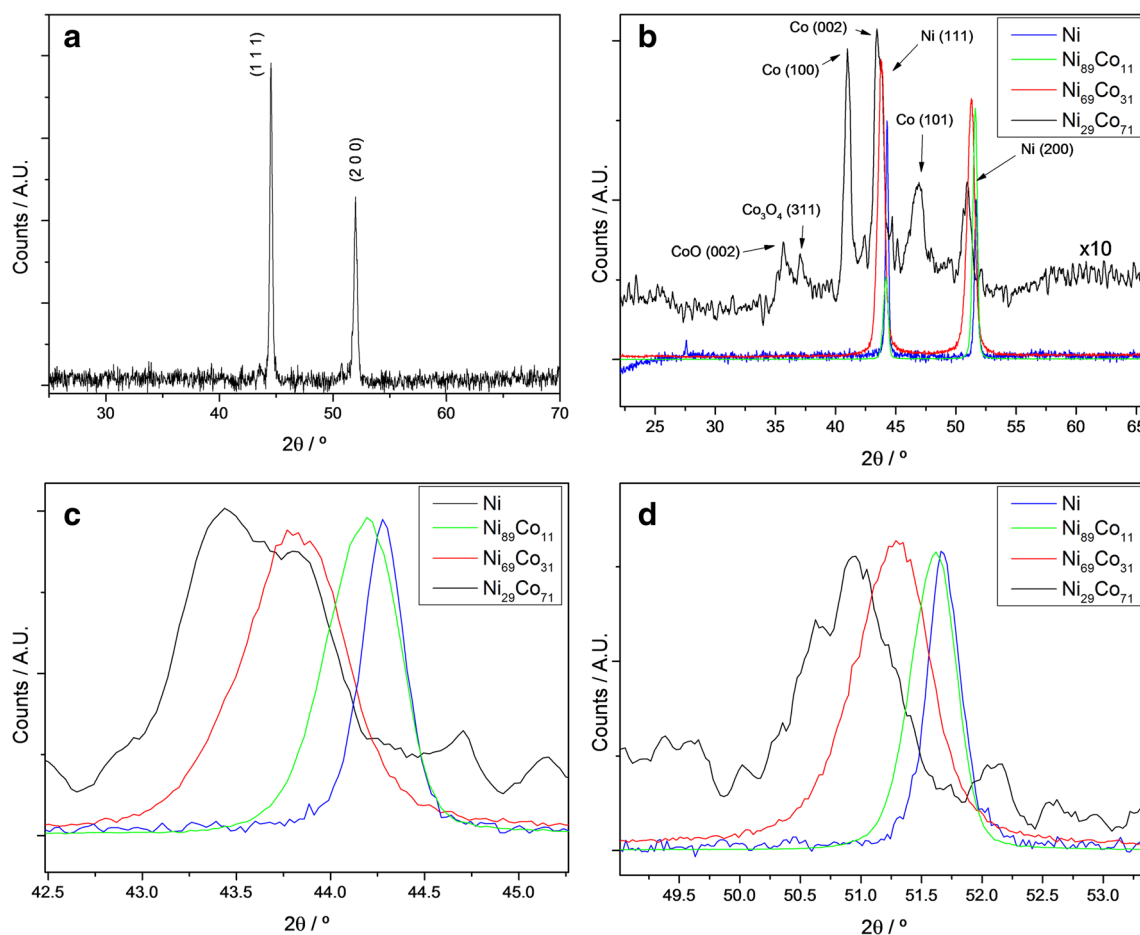

Fig. 2 X-ray diffraction pattern of **a** nickel adhesion layer; **b** Ni Watts, $Ni_{89}Co_{11}$, $Ni_{69}Co_{31}$, and $Ni_{29}Co_{71}$ catalytic layers; **c** zoom of the normalized (1 1 1) peaks of all catalysts; and **d** zoom of the normalized (2 0 0) peaks of all catalysts

Table 2 XRD parameters. Peak position (2θ), full width at half maximum, and d-spacing for each nickel peak on the synthesized catalysts
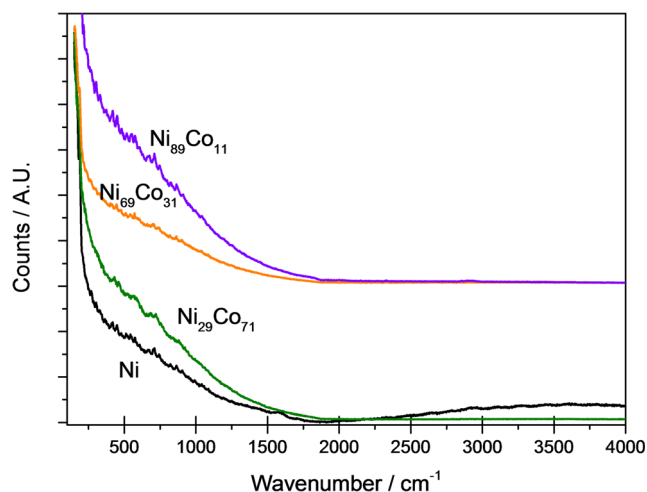
	2θ	FWHM/°	Crystal size/nm	d/Å	Plane
Ni	44.28	0.265	33.82	2.04	(1 1 1)
$Ni_{89}Co_{11}$	44.19	0.468	19.13	2.04	(1 1 1)
$Ni_{69}Co_{31}$	43.80	0.676	13.22	2.07	(1 1 1)
$Ni_{29}Co_{71}$	43.81	0.305	29.36	2.07	(1 1 1)
Ni	51.67	0.295	31.23	1.77	(2 0 0)
$Ni_{89}Co_{11}$	51.62	0.437	21.08	1.77	(2 0 0)
$Ni_{69}Co_{31}$	51.32	0.722	12.76	1.78	(2 0 0)
$Ni_{29}Co_{71}$	50.94	0.864	10.64	1.79	(2 0 0)

observed in the spectra for all catalysts even from different areas of the surface. The scattering spectra from the Ni Watts electrode do not show peaks, indicating that nickel is in a metallic state. Similar spectra are observed for all the Ni_xCo_y catalysts.

Potentiodynamic Analysis

Figure 4a shows the comparison of the potentiodynamic response in 1 M KOH solutions for the synthesized catalysts (pure nickel and nickel-cobalt alloys) measured at 298 K and 5 mV s^{-1} scan rate. It can be seen that the Ni_xCo_y catalyst with a high cobalt content, such as $Ni_{29}Co_{71}$, shows a low current density for HER, even lower than that observed with nickel Watts electrodes, which could be due to the proportion of Co, since it is a poor catalyst for HER [20].

In addition, the current density of $Ni_{69}Co_{31}$ catalyst at − 1.5 V (vs. SCE) is 30% higher than that from $Ni_{89}Co_{11}$ and 112% higher than that from nickel Watts electrodes. The same tendency is observed when the experiments are performed at a

Fig. 3 Raman spectra of freshly synthesized Ni, $Ni_{89}Co_{11}$, $Ni_{69}Co_{31}$, and $Ni_{29}Co_{71}$ catalysts

temperature of 323 K (Fig. 4b). Furthermore, at 323 K, a clear increase about 55% in the average current density, with respect to the values measured at 298 K, is found. Figure 4c shows a zoom of the cyclic voltammogram in the potential zone between − 1.2 and − 0.3 V (vs. SCE), measured at 298 K and 5 mV s^{-1} scan rate. A clear evidence of hydride/hydroxide formation and decomposition is seen, by the presence of current peaks in the potentiodynamic profile with nickel Watts catalysts. However, additional components are present in the same potential region, with all the Ni_xCo_y alloys, possibly due to oxides and/or hydroxides of cobalt. This conclusion is confirmed by successive Raman experiments of the catalysts' surface recorded in ex situ configuration after the aging process (see "Chronoamperometry for aging treatment" section). The Ni Watts sample shows the conventional oxidation current peaks of NiO_x and α-$Ni(OH)_2$ [29], while samples containing Co also exhibit peaks from $Co(OH)_2$ [30].

Figure 4d shows the Tafel plots performed from the data obtained by the cyclic voltammetries measured (Fig. 4a) at 5 mV s^{-1} and 298 K. Nickel Watts, $Ni_{89}Co_{11}$, and $Ni_{69}Co_{31}$ catalysts exhibit a similar Tafel behavior with small variations in the equilibrium potential, whereas the $Ni_{29}Co_{71}$ catalyst exhibits a completely different behavior. This is because this catalyst forms oxides and hydroxides rapidly in alkaline medium, even at low overpotentials, so the observed electrochemical features do not correspond only to the generation of hydrogen but to a combination of processes. This is reflected in the cyclic voltammetry presented in Fig. 3a, where for the $Ni_{29}Co_{71}$ catalyst for hydrogen evolution, commonly evidenced with a continuous growing current—such as those found in Ni Watts, $Ni_{89}Co_{11}$, and $Ni_{69}Co_{31}$ catalysts—is not observed. The samples showed a Tafel slope close to − 0.13 V dec^{-1} normally associated to the Volmer reaction with the transference of one electron as the rate-determining step [31]. The exchange current values (j_0) obtained at 298 K are presented in Table 3. It can be seen that in the cases of the $Ni_{89}Co_{11}$ and $Ni_{69}Co_{31}$ catalysts, the j_0 obtained values are higher than those presented for Ni Watts electrodes. In the particular case of the $Ni_{29}Co_{71}$ catalysts, the Tafel parameters could not be obtained because there is no observed clear slope in the Tafel plot but fluctuations that could be due to the continuous changes happening in the catalyst surface related to the formation and decomposition of Co hydroxides and oxides. This supposition is reinforced by the Raman measures presented in the "Chronoamperometry for aging treatment" section on catalysts subjected to hydrogen generation. On the other hand, this catalyst does not generate the release of hydrogen, which can be evidenced in Fig. 4a, b where, unlike the other catalysts synthesized in this work, the $Ni_{29}Co_{71}$ does not present a hydrogen evolution current, but the current reaches a limit value.
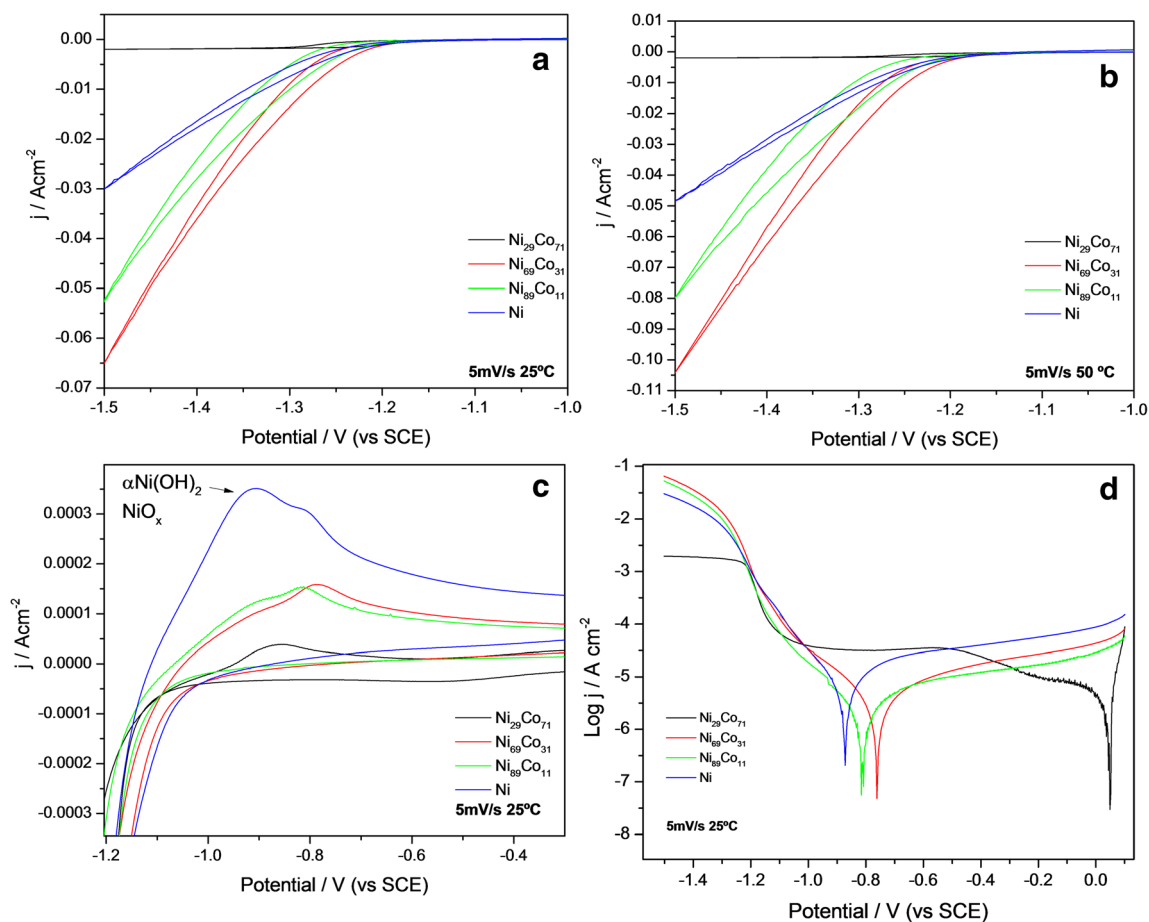
Fig. 4 Cyclic voltammogram of Ni, $Ni_{89}Co_{11}$, $Ni_{69}Co_{31}$, and $Ni_{29}Co_{71}$ catalysts in 1 M KOH at a scan rate of 5 mV s^{-1} at **a** 298 K and **b** 323 K. **c** Magnification of the cyclic voltammogram measured at 298 K. **d** Tafel plots for all the catalysts at 298 K

Chronoamperometry for Aging Treatment

In order to establish the stability of the catalysts, aging experiments at controlled potentials were carried out. Figure 5a shows the chronoamperometric profiles measured at 298 K in 1 M KOH when the applied potential was − 1.5 V (vs. SCE) for all the catalysts synthesized. It can be seen that the $Ni_{89}Co_{11}$ catalyst has a higher catalytic activity after 4 h than the other catalysts analyzed. In order to compare the catalytic activity, a comparison of the current densities reached after 4 h in the chronoamperometric experiment versus the percentage of cobalt in each catalyst is presented in Fig. 5b. The catalytic

activity for HER decreases with the Co content in the alloy after the aging of the electrodes. It is at all far superior to that obtained with pure nickel electrodes.

It is observed that at short times (less than 2000 s), the catalyst $Ni_{69}Co_{31}$ has a higher current density similar to what is observed in the cyclic voltammetry. This increase in current density could be due to the reduction of the cobalt oxides on the surface of the catalyst formed due to hydrogen generation leaving the $Ni_{89}Co_{11}$ catalyst free of surface oxides, a state in which the catalyst is most active. After the aging of the catalysts, the cyclic voltammetric experiments were repeated in order to analyze the changes in the processes occurring on

Table 3 Deactivation rate, Tafel slope (b), exchange current density (j_0), and current densities measured at − 1.5 V (vs. SCE) in a cyclic voltammetry at 5 mV s^{-1}

	δ/s^{-1}	$-b$/mV dec^{-1}	j_0/mA cm^{-2}	Current density[a]	Current density[b]
Ni	3.13×10^{-5}	0.146	0.0015	− 0.030	− 0.026
$Ni_{89}Co_{11}$	-9.11×10^{-4}	0.125	0.0072	− 0.066	− 0.073
$Ni_{69}Co_{31}$	1.00×10^{-3}	0.142	0.0355	− 0.053	− 0.036
$Ni_{29}Co_{71}$	7.82×10^{-4}	No data	No data	− 0.002	− 0.002

[a] Fresh catalysts

[b] Aged catalysts

Fig. 5 **a** Chronoamperometric profile of hydrogen evolution reaction on Ni, $Ni_{89}Co_{11}$, $Ni_{69}Co_{31}$, and $Ni_{29}Co_{71}$ in 1 M KOH obtained at -1.5 V (vs. SCE), 298 K. **b** Correlation of the obtained current densities at 4 h with the cobalt concentration in the catalyst

the electrode due to surface changes. It can be seen in Fig. 6a that the $Ni_{89}Co_{11}$ catalyst after the aging process shows a considerable increase in the modulus of the current density at -1.5 V (vs. SCE), while in the other catalysts, a decrease
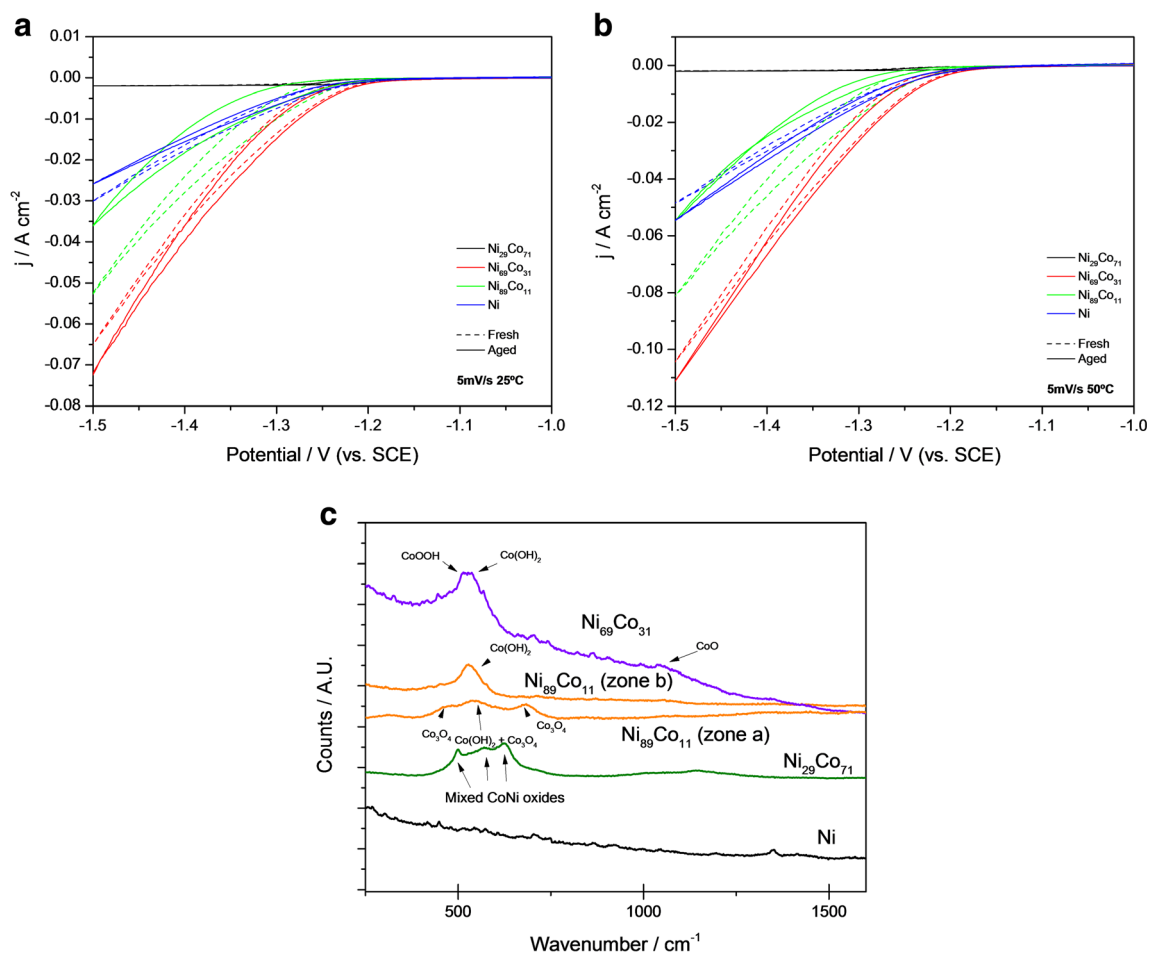

Fig. 6 Cyclic voltammogram before and after the short aging process of Ni, $Ni_{89}Co_{11}$, $Ni_{69}Co_{31}$, and $Ni_{29}Co_{71}$ catalysts in 1 M KOH at a scan rate of 10 mV s^{-1} at **a** 298 and **b** 323 K. **c** Raman spectra of the aged Ni, $Ni_{89}Co_{11}$, $Ni_{69}Co_{31}$, and $Ni_{29}Co_{71}$ catalysts
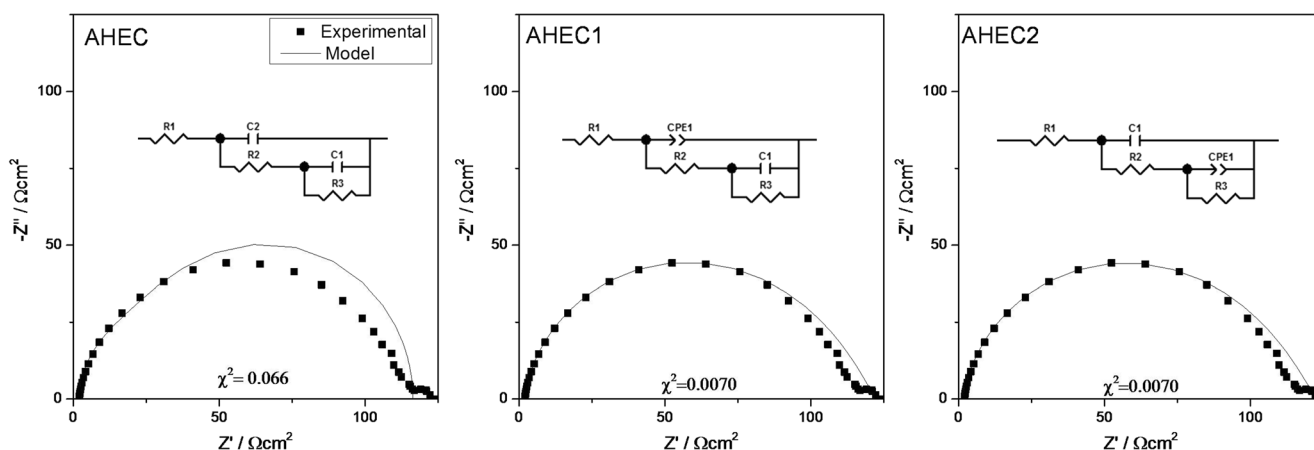
Fig. 7 $Ni_{69}Co_{31}$ measured at 298 K and 1.2 V (vs. SCE) adjusted with the equivalent circuit models: **a** Armstrong and Henderson model and **b, c** CPE-modified Armstrong and Henderson models along with the corresponding value of χ^2

in the potentiodynamic current (considering the absolute value) is shown. This particular increase in the current density modulus for $Ni_{89}Co_{11}$ catalyst is consistent with the chronoamperometric results.

The catalyst deactivation rate (δ) was calculated as presented elsewhere [32, 33]:

$$\delta = -\frac{100}{j_e}\left(\frac{dj}{dt}\right) \qquad (1)$$

where j_e is the current extrapolated at the polarization start, and the dj/dt slope is evaluated from the linear decay at times higher than 2000 s. The deactivation rates of each of the electrodes are presented in Table 3. The current decay rates for Ni_xCo_y catalysts are similar to those found in nickel Watts, except for the $Ni_{89}Co_{11}$ catalyst where the activation process evidenced in the change of sign in the δ is observed, so that the $Ni_{89}Co_{11}$ catalyst does not only show a higher current density than the other catalysts under conditions of hydrogen generation but also is activated with time, at least in the first hours of use.

Figure 6b shows the cyclic voltammetries measured for all the catalysts, fresh and aged, at 5 mV s^{-1} and a temperature of 323 K. It can be seen that the trends are maintained between the different catalysts although with an increase of approximately 55% with respect to the same data measured at 298 K.

Figure 6c shows the Raman spectra of the Ni and Ni_xCo_y samples after aging at − 1.5 V (vs. SCE). The spectra are presented in the region from 250 to 1500 cm^{-1} in order to observe more clearly the cobalt oxide signals. However, no peaks were observed at wavelengths greater than 1200 cm^{-1}, indicating that no nickel hydride or hydroxides were formed during the aging process (usually observed at 3581 and 3660 cm^{-1} [29]).
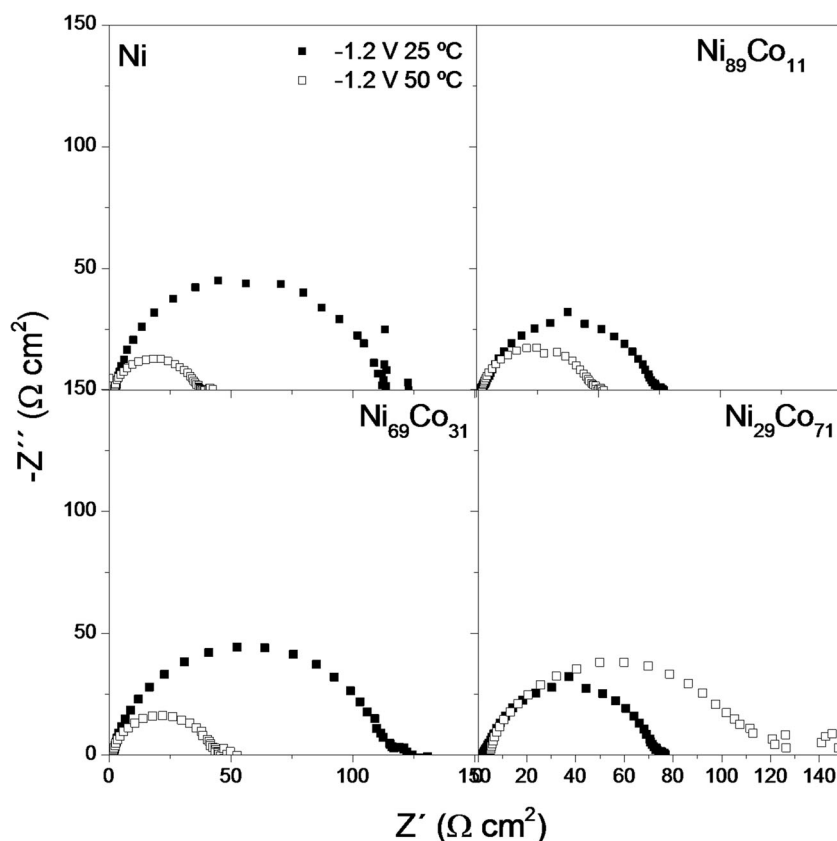
It is well known that cobalt forms oxides and hydroxides in an alkaline medium and that these compounds can be electrochemically reduced to metallic Co or semireduced to oxides

and hydroxides by a potential pulse (similar to that used for the hydrogen generation). Due to the possible oxidation of the deposited cobalt as a consequence of the local alkalinization produced by the HER, we observe the presence of different types and proportions of oxides on the alloy samples. Various spectra from different places on the surface of every sample were recorded. Notably, the spectra from $Ni_{89}Co_{11}$ and $Ni_{69}Co_{31}$ samples present peaks corresponding to $Co(OH)_2$, probably formed by the alkaline medium in which the electrodes were aged (1 M KOH). The $Ni_{69}Co_{31}$ sample shows very low CoO intensity signals and, particularly, the semioxidized CoOOH species. This sample does not show signs of appreciable surface heterogeneities in its composition (measured by Raman spectroscopy). On the other hand, the sample of $Ni_{89}Co_{11}$ presents zones with different Raman spectra. In some areas, the presence of $Co(OH)_2$ is only observed, while in others, the presence of the Co_3O_4 oxide which is commonly found in cobalt electrodes is also observed. The presence of these islands with oxides may be due to differences in the relative content of Ni and Co in the different areas of the sample. Finally, the sample of $Ni_{29}Co_{71}$ presents mixed cobalt oxides and Ni with bands. This is probably due to the fact that nickel is intercalated in the structure of the Co (which is the major component in the catalyst) modifying the

Table 4 Parameters of Nyquist diameter at − 1.2 V (vs. SCE)

Cat./temp.	Nyquist diameter HF (Ω cm^{-2})	
	298 K	323 K
Ni	109.2	34.4
$Ni_{89}Co_{11}$	67.4	46.7
$Ni_{69}Co_{31}$	113.6	41.7
$Ni_{29}Co_{71}$	188.8	121.3

Fig. 8 Nyquist plot impedance spectra in the complex plane for the HER in 1 M KOH at 298 and 323 K and at − 1.2 V (vs. SCE) measured for all the synthesized catalysts

EIS Measurements

It has been widely reported in the literature that the electrical behavior of HER on nickel electrodes in alkaline medium can be adjusted with the Armstrong and Henderson equivalent circuit (AHEC) [34, 35]. This model describes that the HER can be fitted by two circles in the complex plane of the Nyquist plot [36, 37]. Theoretically, those two semicircles correspond to one semicircle at high frequency related to the porosity of the interface and another one at low frequency, associated with the charge-transfer process [37–40], whose values depend on the applied overpotential. However, the AHEC model is not adequate for porous or very rough electrodes [41]. In these cases, it is necessary that there is an addition of a constant phase element (CPE) since experimentally only a single remarkably flattened

spectrum. It is also important to note that no sample shows hydride peaks or nickel hydroxides, which explains that the catalysts are not deactivated as commercial nickel does [29]. No bands corresponding to NiO usually observed at around 402, 559, 735, 901, 1107, and 1594 cm^{-1} were observed, although the oxide bands corresponding to the $Ni_{29}Co_{71}$ catalyst could be a syncretism of the Ni oxides and the Co oxides forming mixed Ni-Co oxides.

semicircle is observed. Furthermore, the use of the CPE for rough electrodes is clearly necessary due to capacitance dispersion [41]. Thus, the AHEC model modified with a CPE component (AHEC1) describes a simple hydrogen evolution process, found usually on polycrystalline Ni and some Ni-based porous electrodes [42–44]. Moreover, on porous electrodes, the high-frequency part of the complex plane plots usually shows either a straight line at 45° or a semicircle for cylindrical or pear shape pores, respectively [38].

Furthermore, the addition of a second CPE to the AHEC model (AHEC2 model) is usually used to improve the fit of the high-frequency semicircle related to the surface roughness of the electrode, with respect to the fitting obtained for the AHEC and AHEC1 models.

The models of equivalent circuits for the adjustments are inserted in Fig. 7 for the $Ni_{69}Co_{31}$ catalyst measured at 298 K and –1.2 V (vs. SCE). A similar fitting was carried out for all the synthesized catalysts. Circuits with CPE components have given the best fit of data, obtaining the lowest χ^2 values. In our particular case, it was taken as a measure of the goodness of the fitting a χ^2 value lower than 0.01. When χ^2 value is lower than 0.01, it can be said that the deviation of the adjustments from the data obtained is less than or equal to 1% [45].

To obtain capacitance values, when using constant phase element, posterior calculations are necessary.

Taking into account that the impedance for a CPE at the interface is as follows [41]:

$$Z_{CPE} = \frac{1}{T(j\omega)^{\phi}}$$

where T is a capacitance parameter (F cm^{-2} s$^{\phi-1}$) and $\phi \leq 1$ is a parameter that characterizes the rotation of the complex plane in the impedance graph to fit the flat semicircles. For the calculation of the double layer capacitance from a constant phase element, the following equation [41] was used in case of using nonideally polarizable surfaces on the AHEC2 model.

$$T = C_{dl}^{\phi}\left(R_s^{-1} + R_{ct}^{-1}\right)^{1-\phi}$$

All the capacitance and resistance data obtained for the different catalysts and models are presented in the Supplementary Information, together with the χ^2 values obtained for each fitting.

It is observed that the R_{ct} decreases with the applied overpotential and that these values are lower in the Ni$_{89}$Co$_{11}$ and Ni$_{69}$Co$_{31}$ catalysts than in the Ni Watts catalyst, which is consistent with the higher catalytic activity of those catalysts.

The diameters of the Nyquist plots were evaluated in the low-frequency zone (Table 4), which were related with the charge transfer processes [41] at -1.2 V (vs. SCE), where the hydrogen evolution is already advanced. At lower values of this diameter, a greater activity is expected for the electrocatalyst since it decreases the associated charge transfer resistance [44] (Fig. 8).

It can be seen how the Nyquist diameter values decrease with increasing temperature, promoting an increase in the current density for the hydrogen evolution reaction [46]. For measurements at 298 K, a decrease in the Nyquist diameter is observed when the percentage of cobalt in the alloy decreases, in agreement with the current densities recorded at 298 K during chronoamperometry.

Conclusions

In this work, we have obtained excellent Ni$_x$Co$_y$ alloy catalysts for HER through galvanostatic electrodeposition on 316L steel. Deposits with different compositions of the deposit were formed by electrodeposition employing different Ni/Co ratios in the electrodeposition bath.

Optimization of the polishing and cleaning processes of the 316 L steel surface was carried out and subsequent Ni adherent layer was also required before the electrodeposition of the alloy. We find that every step on the protocol must be properly performed in order to prepare the surface for the very uniform electrodeposits of catalytic layers.

Ni$_x$Co$_y$ catalysts were obtained using nominal compositions of Co in the electrodeposition bath as low as 1.5 to

3.5%, so it is possible to obtain Ni$_{89}$Co$_{11}$ and Ni$_{69}$Co$_{31}$ alloys practically without modifying the properties of the electrodeposition bath. These alloys give hydrogen current densities up to 112% higher than those presented with deposited nickel from Ni Watts.

The catalysts presented in this work are an economical and scalable alternative for the replacement of the catalysts currently used in alkaline electrolyzers. The use of 316 L steel allows avoiding corrosion in case of fractures in the catalytic layer. In this way, the electrodeposition process allows to substantially lower the cost of electrodes, up to 63% of the cost of conventional solid Ni electrodes currently used in electrolyzers (according to the costs of materials in Argentina, 2017).

References

1. R. Carnieletto, J.B. Parizzi, F.A. Farret, C.G. Ribeiro. Latin America Conference and Exposition (2012) https://doi.org/10.1109/TDC-LA.2012.6319133
2. M. Higuita Cano, K. Agbossou, S. Kelouwani, Y. Dube, Renew. Energ. **113**, 1086 (2017)
3. R. Carnieletto, J.B. Parizzi, A.C. Schittler, F.A. Farret. Industrial Technology (ICIT) (2010). https://doi.org/10.1109/ICIT.2010.5472602
4. P. Artuso, R. Gammon, F. Orecchini, S.J. Watson, Int. J. Hydrogen Energ. **36**, 7956 (2011)
5. D. Ferrero, M. Santarelli, Energ. Convers. Manage **148**, 16 (2017)
6. M. Carmo, D.L. Fritz, J. Mergel, D. Stolten, Int. J. Hydrogen Energ. **38**, 4901 (2013)
7. P. Millet, R. Ngameni, S.A. Grigoriev, N. Mbemba, F. Brisset, A. Ranjbari, C. Etievant, Int. J. Hydrogen Energ. **35**, 5043 (2010)
8. R. Orinakova, A. Turonova, D. Kladekova, M. Galova, R. Smith, J. Appl. Electochem. **36**, 957 (2006)
9. M. Meyers, A. Mishra, D.J. Benson, Prog. Mater. Sci. **51**, 427 (2006)
10. E. De Las Heras, D.A. Egidi, P. Corengia, D. Gonzalez-Santamaria, A. García-Luis, M. Brizuela, G.A. Lopez, M. Flores Martinez, Surf. Coat. Technol. **202**, 2945 (2008)
11. H. Dong, P.Y. Qi, X.Y. Li, R.J. Llewellyn, Sci. Eng. A **431**, 137 (2006)
12. J.C. Puippe, F. Leaman, *Theory and Practice of Pulse Plating* (American Electroplaters and Surface Finishers Soc, Orlando, 1986), p. 1
13. A.N. Correia, S.A.S. Machado, J. Appl. Electrochem. **33**, 367 (2003)
14. A.N. Correia, S.A.S. Machado, Electrochim. Acta **45**, 1733 (2000)
15. A. Brenner, *Electrodeposition of Alloys Principles and Practice* (Academic, London, 1963), p. 1
16. E. Gomez, S. Pane, E. Valles, Electrochim. Acta **51**, 146 (2005)
17. D. Landolt, J. Electrochem. Soc. **149**, S9 (2002)

18. Y. Li, H. Jiang, W. Lou, L. Wang, Electroplating and Finishing. **9**, 1 (2008)

19. W.E.G. Hansal, B. Tury, M. Halmdienst, M. Lakatos Varsanyi, W. Kautek, Electrochim. Acta **52**, 1145 (2006)

20. C. Lupi, A. Dell'Era, M. Pasquali, Int. J. Hydrogen Energ. **34**, 2101 (2009)

21. M. Granada, C.I. Elsner, A.R. Di Sarli, Analisis Comparativo de Diferentes Metodologías de Limpieza en Aceros HDG (16° Congreso Internacional de Metalurgia y Materiales, 2016), http://sam-conamet2016.congresos.unc.edu.ar/2016/11/29/libro-de-resumenes/. Accessed 04 January 2018

22. J. Rodríguez-Carvajal, Physica B **192**, 55 (1993)

23. E.A. Franceschini, G.I. Lacconi, H.R. Corti, Electrochim. Acta **159**, 210 (2015)

24. A. Bai, C.C. Hu, Electrochim. Acta **47**, 3447 (2002)

25. D.G. Lamas, M. de Oliveira Neto, G. Kellermann, A.F. Craievich, in Nanocharacterization Techniques, ed. By O. de Oliveira; M.L.G. Ferreira, F. de Lima Leite, A.L. da Róz (William Andrew Publishers, Verlag, 2017) pp. 111

26. R.E. Smallman, A.H.W. Ngan, *Physical Metallurgy and Advanced Materials Engineering*, 7th edn. (Butterworth-Heinemann, Oxford, 2007), p. 161

27. K.M. Shaju, L. Guerlou-Demourgues, G. Godillot, F. Weill, C. Delmas, J. Electrochem. Soc. **159**, A1934 (2012)

28. K. An, N. Lee, J. Park, S.C. Kim, Y. Hwang, J.G. Park, J.Y. Kim, J.H. Park, M.J. Han, J. Yu, T. Hyeon, J. Am. Chem. Soc. **128**, 9753 (2006)

29. D.S. Hall, C. Bock, B.R. MacDougall, J. Electrochem. Soc. **160**, F235 (2013)

30. E.M. Garcia, V.F.C. Lins, T. Matencio, In Modern Surface Engineering Treatments; ed. by Mahmood Aliofkhazraei (InTech, London, 2013) pp. 101

31. E.A. Franceschini, G.I. Lacconi, H.R. Corti, Int. J. Hydrogen Energ. **41**, 3326 (2016)

32. E.A. Franceschini, M.M. Bruno, F.J. Williams, F.A. Viva, H.R. Corti, ACS Appl. Mater. Interfaces **5**, 10437 (2013)

33. M.M. Bruno, E.A. Franceschini, G.A. Planes, H.R. Corti, J. Appl. Electrochem. **40**, 257 (2010)

34. R.D. Armstrong, M. Henderson, J. Electroanal. Chem. **39**, 81 (1972)

35. E.A. Franceschini, G.I. Lacconi, H.R. Corti, J. Energy Chem. **26**, 466 (2017)

36. E. Daftsis, N. Pagalos, A. Jannakoudakis, P. Jannakoudakis, E. Theodoridou, R. Rashkov, M. Loukaytsheva, N. Atanassov, J. Electrochem. Soc. **150**, C787 (2003)

37. J. Panek, A. Serek, A. Budniok, E. Rowinski, E. Lagiewka, Int. J. Hydrogen Energ. **28**, 169 (2003)

38. A. Lasia, In Modern Aspects of Electrochemistry, ed. B.E. Conway, R.E. White (Kluwer/Plenum, New York, 2002) pp. 143

39. R.K. Shervedani, A. Lasia, J. Electrochem. Soc. **144**, 2452 (1997)

40. R.K. Shervedani, A. Lasia, J. Appl. Electrochem. **29**, 979 (1999)

41. Z. Kerner, J. Pajkossy, Electrochim. Acta **46**, 207 (2000)

42. A. Lasia, A. Rami, J. Electroanal. **294**, 123 (1990)

43. A. Lasia, Curr. Topics Electrochem. **2**, 239 (1993)

44. L. Chen, A. Lasia, J. Electrochem. Soc. **138**, 3321 (1991)

45. J.F. Kenney, E.S. Keeping, *Mathematics of Statistics*, 2nd edn. (Princeton, New Jersey, 1951)

46. P. Barbaro, C. Bianchini, in *Catalysis for Sustainable Energy Production*, ed. by B. E. Guerrini, S. Trasatti. (Weinheim, Wiley, 2009)